# Simplified 1-D calculation of 13.5-nm emission in a tin plasma including radiation transport

J. White,[a)1] P. Dunne,[1] P. Hayden,[2] and G. O'Sullivan[1]

*1 School of Physics, University College Dublin, Belfield, Dublin 4, Ireland*

*2 School of Physical Science, Dublin City University, Dublin 9, Ireland*

Many next generation lithography schemes for the semiconductor industry are based on a 13.5-nm tin plasma light source, where hundreds of thousands of *4d-4f*, *4p-4d*, and *4d-5p* transitions from $Sn^{5+}$–$Sn^{13+}$ ions overlap to form an unresolved transition array. To aid computation, transition arrays are treated statistically, and Hartree-Fock results are used to calculate radiation transport in the optically thick regime with a 1-D Lagrangian plasma hydrodynamics code. Time-dependent spectra and conversion efficiencies of 2% in-band 13.5-nm emission to laser energy are predicted for a Nd:YAG laser incident on a pure tin slab target as a function of laser power density and pulse duration at normal incidence. Calculated results showed a maximum conversion efficiency of 2.3% for a 10-ns pulse duration at $8.0 \times 10^{10}$ W/cm$^2$ and are compared to experimental data where available. Evidence for the need to include lateral expansion is presented.

## I. INTRODUCTION

The current semiconductor manufacturing lithographic source wavelength is 193 nm, produced by an ArF excimer laser, resulting in sub-100-nm feature sizes. To continue manufacturing integrated circuits in keeping with past industry improvements[1] and extend beyond the 32-nm node, a 13.5-nm (91.8-eV) laser-produced plasma (LPP) or discharge pulsed plasma (DPP) extreme ultraviolet (EUV) source is suggested.[2,3] For industry purposes, the conversion efficiency (CE) for LPP or DPP sources is calculated within a 2% bandwidth at 13.5 nm, which corresponds to the maximum reflectivity of the Mo/Si multi-layer mirrors used in the manufacturing tool.[1] Although various materials such as Sn, Xe, O, Li, and F ions[4] emit in the 13–14-nm region, most work is concentrated on tin, because of its high CE potential.[5–7]

Two major commercial lasers are also still under consideration for use in next generation lithography high volume manufacturing: the 1.064-μm wavelength Nd:YAG laser and the 10.6-μm wavelength $CO_2$ laser, or a combination thereof (as in a Nd:YAG pre-pulse to prime the plasma followed by a $CO_2$ main pulse). Most modelling to date has been done with Nd:YAG laser LPPs, and there is an abundance of experimental data for benchmarking. Here, we calculate CE as a function of operating parameters for a tin LPP produced by the Nd:YAG laser to compare to experiment at University College Dublin (UCD) and elsewhere, and to benchmark future modelling. Observations are made about $CO_2$ LPPs where applicable and the methodology discussed here will be applied to other systems in a future paper.

An unresolved transition array (UTA) can be the strongest feature in EUV LPP spectra, consisting of thousands of transitions between bands of near-degenerate energy levels.[8-10] The complexity of the configurations is such that a line-by-line analysis is computationally extremely intensive and statistical methods can be used to reduce its complexity for computational purposes,[11–13] where the UTA is represented as a Gaussian profile characterised by three parameters: position ($\mu_1$), width ($\sigma$), and summed weighted oscillator strength ($\Sigma gf$).

In a previous paper[13] we calculated UTA statistics for the main contributing 13.5-nm tin ions in the optically thin regime, which showed a maximum in-band (13.5 nm ± 1%) emission from $Sn^{8+}$ – $Sn^{12+}$ for a plasma electron temperature of 40 eV. Weighted dipole oscillator strengths versus wavelength were calculated from a Hartree-Fock configuration interaction (HFCI) code[11] and weighted by fractional ion density using a steady-state plasma model.[14] In another paper,[15] we calculated the $4p^6 4d^N$, $4p^6 4d^{N-1} 4f^1$ + $4p^5 4d^{N+1}$, and $4p^6 4d^{N-1} 5p^1$ ($N$ = 1-9) time-dependent population levels for $Sn^{5+}$ – $Sn^{13+}$ using the statistical representation of the ion mean energies,[13] and an energy functional method to interpolate between the $l$-degenerate population levels.[16] In this paper, the statistically simplified UTA parameters and the $nl$-level populations are used in radiation transport calculations to determine the resultant emission in an optically thick plasma, with significant computational savings.

It should be noted that Sasaki *et al*.[17] used the UTA approach to deal with weaker transitions in an earlier paper; however there are a number of differences between their method and that of the present work. They include dielectronic recombination and satellite emission. Moreover, they assumed local thermodynamic equilibrium (LTE) and

used the HULLAC code with a complete line-by-line description for the strongest transitions, whereas we use collisional-radiative (CR) equilibrium and a full UTA treatment. The present work is a considerable simplification of their approach, of which the differences and outcomes will be dealt with as they arise. Comparisons are also made to experiment where applicable, highlighting the differing setup parameters, such as wavelength, pulse duration, power density, target material and geometry.

## II. UNRESOLVED TRANSITION ARRAY STATISTICS

To estimate the emission from tin ions in the 2% bandwidth centred on 13.5 nm, the distribution of weighted dipole oscillator strength ($gf$) versus wavelength ($\lambda$) was calculated for *4d-4f*, *4p-4d*, and *4d-5p* transitions in $Sn^{6+} - Sn^{13+}$ ions using the COWAN HFCI suite of codes.[11] Because of the large number of transitions, statistical methods were used to calculate the UTA mean and width,[12,18] which were then weighted by ion distribution within the LPP[14] to estimate the steady-state spectral profile.[13]

For each ion, an UTA is characterized by position and width,[11,12] where the mean ($\mu_1$) and noncentred variance ($\mu_2$) are given by Eq. 1 and the area is equal to the summed weighted oscillator strength ($\Sigma gf$).[13] UTA emission and absorption can then be statistically represented by a Gaussian profile for each transition type (*e.g.*, *4d-4f* and *4p-4d*), as in Eq. 2, based on the leading eigenvalue percentages in the HFCI calculation.[13] The statistical UTAs can then be added together as separate Gaussians and weighted by ion fraction, determined either by a steady-state or time-dependent model, where in the time-dependent case the problem reduces to determining the spatial and temporal ion

fractions within the plasma. Note that the standard deviation, $\sigma$, is used instead of the variance in the Gaussian representation.

$$\mu_n = \frac{\sum_{i=1}^{N} (\lambda_i)^n gf_i}{\sum_{i=1}^{N} gf_i} \tag{1}$$

$$f(x) = \frac{1}{\sigma\sqrt{2\pi}} e^{-\frac{(x-\mu_1)^2}{2\sigma^2}} \tag{2}$$

Two representative statistical UTAs are shown in Fig. 1 for *4d-4f* and *4p-4d* transitions in $Sn^{10+}$ and $Sn^{11+}$, where a reduced width, $\sigma'$, was used because of the numerous small-oscillator strength outliers ($gf << 1$).[13] It is well known that for these transitions, the upper $4p^6 4d^{N-1} 4f + 4p^5 4d^{N+1}$ configurations are highly mixed, yet it is instructive to separate the transitions based on the leading eigenvalue percentages. As previously presented,[13] the statistical UTA parameters ($\mu_1$, $\sigma'$, $\Sigma gf$) can effectively represent UTA emission profiles at different electron temperatures and densities in the plasmas considered here.

## III. PLASMA HYDRODYNAMICS, THE AVERAGE ATOM MODEL, THE ENERGY FUNCTIONAL AND *nl*-LEVEL POPULATIONS

A plasma is characterized by electron/ion densities and electron/ion temperatures within it. In the optically thin, steady-state case, an average electron temperature at a given electron density can be calculated for a given laser pulse power density, $\phi$, from which the ion distribution ($f_z$ versus charge state $z$) can be calculated using rate equations for collisional ionisation, radiative recombination, and three-body recombination.[14] For such a steady-state tin plasma, the maximum in-band radiation was calculated at 40 eV for $\phi = 7 \times 10^{10}$ Wcm$^{-2}$, giving $Sn^{10+}$ as the dominant ion.[13]

For an optically thick plasma, however, radiative output depends on the differing opacities in the plasma, where radiation from the core can be absorbed and re-emitted many times.[19] The spatial and temporal hydrodynamics must be calculated using non-LTE equations to calculate electron temperature and free electron density as a function of position and time. Using the 1-D Lagrangian, finite difference, laser-matter interaction program MED103,[20] the ion fraction and *l*-degenerate level populations can be determined over the 400-cell (10-μm initial width) simulation.

An energy functional method,[16] which interpolates between the *l*-degenerate levels, and a statistical Gaussian representation of the ion mean energies, are used to calculate the $4p^6 4d^N$, $4p^6 4d^{N-1} 4f^1$, $4p^5 4d^{N+1}$, and $4p^6 4d^{N-1} 5p^1$ configuration populations for the distribution of states with different *nl* levels (*nl* splitting required for 4-4, $\Delta n = 0$ transitions). To calculate the *nl* level populations of an ion, the average atom energy functional form of the reduced population probability is used, rather than explicitly determining levels and their corresponding populations, as described in Ref. 15. The occupation numbers, $P_n$, are calculated from MED103[20,21] and the *l*-degenerate level energies calculated from the screened hydrogenic model.[22] The *nl*-level populations are

then calculated from the energy functional at the corresponding transition energy, $E_{nl}$. An outline of the procedure is given in Ref. 15, where the population number densities, $N_i$ (lower) and $N_j$ (upper), required in radiation transport modelling, are obtained.

For example, the mean UTA energy was calculated as 84.67 eV for $Sn^{9+}$ and the $n = 4$ and $n = 5$ occupation numbers determined from the hydrodynamic code output, from which the corresponding level populations were calculated. From the statistical UTA and the calculated *nl*-level populations, the resultant emission can be estimated.

The population number densities for use in radiation transport modelling are shown in Fig. 2 as a function of distance again for two representative ions, $Sn^{10+}$ and $Sn^{11+}$, at the peak of the pulse as calculated in Ref. 15. Note that an energy functional is constructed for each cell and time for each ion to produce the *nl*-level populations throughout the plasma, a computationally extensive process which is simplified by the statistical UTA approach. Using the calculated level populations, ion densities, emission and absorption profiles, and the absorbing cell lengths and velocities, radiation transport within an optically thick plasma can be modelled over the entire plasma with significant computational savings.

## IV. RADIATION TRANSPORT MODELLING

The rate equations included in the calculation are those for electron collisional excitation and de-excitation, electron ionisation, three-body recombination, spontaneous emission, and radiative recombination.[23] As already discussed, *nl* splitting for $\Delta n = 0$ (and

*4d-5p*) transitions is determined using the energy functional method,[16] from which the $4p^6 4d^N$, $4p^6 4d^{N-1} 4f^1$, $4p^5 4d^{N+1}$, and $4p^6 4d^{N-1} 5p^1$ ($1 \leq N \leq 9$) level populations are calculated. From the *nl* level populations of the contributing ions, emissivities and opacities of the fluid cells are then calculated to determine the multi-frequency radiation transport through the plasma, to give a spatially and temporally resolved spectrum and conversion efficiency in the 13.5-nm range.

The methodology for calculating radiation transport in an optically thick plasma is described in Refs. 23–25, and is only summarised below. A schematic of the cross section through a cylinder is shown in Fig. 3.[23] The laser pulse is incident on the target from the right, where $\Delta z_m$ is the cell width, $v_m$ the velocity, and the angle to the incident laser pulse for cell $m$ is equal to zero (normal incidence).

The radiative transfer equation is given in Eq. 3.[26]

$$\frac{\partial I_\nu}{\partial z} = K_\nu I_\nu + E_\nu \tag{3}$$

where $K_\nu$ is the absorption coefficient, $I_\nu$ is the intensity, $E_\nu$ is the total emissivity (all functions of frequency $\nu$), and $z$ is the distance.

Eq. 3 can be solved for a range of frequencies at all positions and angles in the plasma, but is computationally very intensive.[26] Instead, an optical thickness, $\tau_\nu$, over the distance from the point of emission to the plasma boundary[24] is defined to simplify the solution. The radiative transfer equation is then given by

$$\frac{\partial I_\nu}{\partial \tau_\nu} = I_\nu - S_\nu \tag{4}$$

where $I_\nu$ is the radiation intensity, $\tau_\nu$ the optical depth, and $S_\nu$ the source function,[23] where $S_\nu = E_\nu/K_\nu$.

The solution to the radiative transfer equation[23] is then given as

$$I_\nu(\tau_\nu) = I_\nu^0 e^{-\tau_\nu} + \int_0^{\tau_\nu} S_\nu(t) e^{-t} dt \tag{5}$$

where the integral is evaluated from $\tau_\nu$ to the edge of the material and $I_\nu^0$ is the incident radiation intensity at $\tau_\nu$.

For a homogeneous plasma with no incident radiation, the intensity is thus

$$I_m(\nu) = \sum_l S_m^l(\nu)[1 - \exp(\chi_m^l(\nu)\Delta z_m)] \tag{6}$$

where $S^l_m(\nu)$ is the source function and $\chi^l_m(\nu)$ is the opacity of line $l$ and cell $m$ and $\Delta z_m$ the length of cell $m$. The sum is taken over each line. Note that Eq. 6 assumes no line interaction in the emission cell.

The source function at a given frequency, $\nu$, for line $l$ and cell $m$ is

$$S_m^l(\nu) = \frac{2h\nu^3}{c^2}\frac{1}{\left[\frac{N_i g_j}{N_j g_i} - 1\right]} \tag{7}$$

where $S$ is in W/m$^2$/sr[/Hz/s], $N_i$ and $N_j$ are the population number densities in cm$^{-3}$, $g_i$ and $g_j$ are the degeneracies of the $i$th and $j$th levels ($i$ is the lower level and $j$ the higher level), and $h$ and $c$ have their usual meaning. $N_i$ and $N_j$ are calculated as discussed in Sec. III.[15]

The opacity for line $l$ and cell $m$ is

$$\chi_m^l(\nu) = \frac{\pi e^2}{4\pi\varepsilon_0 m_e c} f_{ij} N_i \left[1 - \frac{N_j g_i}{N_i g_j}\right] \phi_m^l(\nu) \tag{8}$$

where $f_{ij}$ is the absorption oscillator strength for an $i$-$j$ transition; ($f_{ij} = gf/(2J_i+1)$). $2J_i + 1$ is the degeneracy and $J_i$ is the total angular momentum of the lower configuration. $\phi^l_m(\nu)$ is the area normalised line profile assumed to be the same in emission and absorption.[24] Lines are not Doppler broadened; however the reduced UTA width due to the large number of outliers is used as described in Ref 15. Note that Stark broadening (which includes electron collision effects) is not necessarily negligible in Sn plasmas[27] and that $N_j << N_i$ (no population inversion) is assumed and thus stimulated emission can be neglected.

The emission profile is then recursively attenuated through successive cells, where the observed emission from cell $m$ is given in Eq. 9.

$$I_m^{obs}(\nu) = I_m(\nu)\exp\left(\sum -\chi_n(\nu)\Delta z_n\right) \tag{9}$$

## V. RESULTS AND COMPARISON WITH EXPERIMENT

Calculated spectra for tin plasmas under different laser power densities and pulse durations are presented and the results compared to experiments undertaken at UCD[28] and those reported in the available literature. The conversion efficiency (CE), defined as the percentage of laser energy converted to in-band radiation, is given in Eq. 10 and used to quantify the optimum laser parameters to produce radiation within a 2% bandwidth (13.5 nm ± 1%). $I_{out}$ is in W/m$^2$/sr[/Hz/s] and is converted to energy by integrating over the simulation time, $t_{stop}$, and the 2% in-band frequency range (calculated over 20 frequency points between 13.365–13.635 nm) and multiplying by the focussed spot radius surface area, $\pi r^2$, and $2\pi$ sr. A constant surface area at the end of the simulation is used.

$$CE = \frac{2\pi \int_{13.5-1\%}^{13.5+1\%} \int_{0}^{t_{stop}} I_{out}(\lambda,t)\,dt\,d\lambda\,dA}{E_{tot}} \qquad (10)$$

The laser energy is calculated using Eq. 11 where $P_{max}$ is the maximum power density, $\tau$ is the pulse duration, $\xi$ is the error function, and $r$ is the focussed spot radius. The ratio of $P_{max}$ to $P_{equiv}$ (to convert from cylindrical to planar geometry) is given in Eq. 12. The plasma length was calculated as the position of the last cell for each time step in MED103.

$$E_{tot} = P_{\max} \tau \frac{\sqrt{\pi}}{2} \cdot \xi \cdot r \qquad (11)$$

$$P_{\max} = \frac{P_{equiv} r}{100} \ [r \text{ in } \mu\text{m}] \qquad (12)$$

A 1100-mJ, Spectron Nd:YAG laser was used in the experiments at UCD.[28] The laser pulse is modelled in the hydrodynamic calculations as a single Gaussian of a given input maximum power density and pulse duration (FWHM) for a 1064-nm laser, which matches the peak, but could more realistically be represented as a sum of four Gaussians (Fig. 4).

1-D spatial output in the direction of the laser pulse (normal incidence) is reported. Absorption from neutral and lower tin ion discrete transitions (Sn I – Sn IV) is not included in the opacity calculations, since absorption from these ions is considerably reduced at normal incidence.[29,30] Doppler shifted absorption from high-velocity gradients is also omitted, as the plasma expansion velocities are not observed to be high enough to have a significant effect (~$10^6$ cm/s). As stated in Sec. I, satellite emission is not included as dielectronic recombination was not calculated in the modelling since the bulk of the satellite emission contributes only to the out-of-band spectra and has minimum effect on the in-band CE.[31,32] Spatially-dependent laser absorption is from inverse bremsstrahlung[33] and is modelled as 20%, the default value in MED103.[20]

Two surveys are presented which independently vary power density and pulse duration. A cylindrical target of 90 μm radius is assumed in all simulations. An

equivalent power density is given in MED103 to convert from cylindrical geometry to planar geometry to compare to data from experimental planar targets.[28]

In the first survey, the power densities are varied from 0.5 to 2.0 x $10^{11}$ W/cm$^2$, with a 15-ns pulse duration (FWHM) at a wavelength of 1064 nm (Nd:YAG). Using the power density with the maximum conversion efficiency (CE) from the first survey, the pulse duration is then varied from 7 to 40 ns (FWHM). The theoretical spectra and a conversion efficiency are calculated for each case and results compared to experiment.[28]

## Varying power density

In the first survey, power density was varied from 0.5 to 2.0 x $10^{11}$ W/cm$^2$. The relevant data is shown in Table I along with some general results (laser energy, CE into $2\pi$ sr, plasma length, maximum electron temperature, $T_e$ and maximum average charge, $\langle z \rangle$). Because of the optically thick nature of the plasma only the outermost cells of the plasma contribute to net in-band emission and thus the results are calculated for a simulation over the outer 20 cells,[34] resulting in a further significant computational saving. Note that a survey of cell number was conducted and the results were almost identical for simulations with greater than 20 cells.

The calculated spectra are shown in Fig. 5. Note that the emission increases and then decreases with increased power density as the emission from contributing ions moves in- and then out-of-band, as was seen in the steady-state case, where an average electron temperature and density was assumed over the whole plasma. As a result the

spectrum narrows as power density increases and net emission decreases. Furthermore, the wavelength at peak emission decreases as power density increases, as seen both experimentally[28] and in the steady-state analysis.[13]

A calculated spectrum for the power density of maximum CE ($0.8 \times 10^{11}$ W/cm$^2$) and corresponding experimental spectrum from Ref. 28 is shown in Fig. 6, where a baseline has been added to the calculated spectra to account for recombination. The baseline is set equal to the experimental intensity at 10 nm, which corresponds to a region of minimum discrete emission. An experimental spectrum ($0.9 \times 10^{11}$ W/cm$^2$) scaled by a factor of 0.94 ($\cos^{0.18}(\pi/4)$) as given in Ref. 28 is included to compare the calculated results at 90° with the experimental results at 45°, where $\theta$ is the angle between laser incidence and the detector. It can be seen that the spectra are well matched on both short and long wavelength sides of the UTA using the non-LTE population levels calculated by the energy functional method. The difference in the peaks can be attributed to the differences between the UTA and the actual emission profiles of each contributing ion stage as well as absorption from Sn I – Sn V ions, especially Sn IV and Sn V[30]. The maximum CE experimental spectrum ($1.6 \times 10^{11}$ W/cm$^2$) is included to highlight the higher power density required to match the 1-D result. Note that by correcting for the continuum contribution the peaks are comparable, where the peak for line emission is about 5 mJ/sr/nm in each case.

A plot of CE versus power density is given in Fig. 7, for the calculated spectra and the experimental spectra in Ref. 28. A maximum calculated CE of 2.21% is observed at $0.8 \times 10^{11}$ W/cm$^2$. Hayden *et al.*[28] observed a maximum CE of 2.28% at $1.6 \times 10^{11}$ W/cm$^2$ for experimental results at 45°. It should be noted that in a real plasma emission is

anisotropic and emission is strongly dependent on observation angle.[25] Thus the calculated CE would be greater than that obtained from a 2-D or 3-D plasma. It has also been reported that experimental CEs are 70% of simulated CEs, because non normal incidence radiation travels $1/\cos(\theta)$ longer and thus absorption is greater.[31] But most importantly, a 1-D simulated plasma does not consider lateral heat transfer or plasma expansion along the target.[31] As such, the calculated plasma reaches optimum electron temperature (30–40 eV) for 13.5-nm emission at a lower power density than experiment because no energy is converted into lateral expansion.

It should be noted that in the simulated spectra, the spot size was kept constant and the energy varied, but that the experimental spot sizes were calculated ± 5%.[28] As well, only *4d-4f*, *4p-4d*, and *4d-5p* UTAs are considered and satellite transitions and absorption from lower ion stages are not included.

Differences between calculation and experiment can be attributed to lateral expansion not accounted for in 1-D codes.[35] Note that lateral expansion occurs when the focal spot size is comparable to the plasma size,[35] however, large spot sizes can be used to limit the effect of energy loss from lateral expansion.[36] Dips in angular distribution of in-band EUV emission can be attributed to 2D expansion,[37] where lateral and longitudinal expansion are of the same scale for smaller spot sizes, but expansion is entirely longitudinal for spot sizes larger than a few hundred microns. Note that in experiments using a 700-mJ, 8-ns Nd:YAG[38] incident on 10-μm diameter mass-limited oxygen-containing targets and 20-μm diameter solid glass $SiO_2$ spheres, the mass-limited droplet expanded much faster and isotropically in 3D compared to 1D expansion in a bulk target.

Plasma length (at the end of the simulation) and maximum electron temperature versus the surveyed power densities are shown in Fig. 8, where it is seen that both depend linearly on laser power density[39] and gives a straightforward indication of the dependence of plasma length (and thus the velocity of expansion) and maximum electron temperature (and thus average charge) on power density. A simple estimate of the optimum power density near 1 x $10^{11}$ W/cm$^2$ can be seen since optimum 13.5-nm emission is between 35 and 40 eV, as reported in the steady-state analysis.[13]

Calculated spectra at selected times near the peak of the pulse (19–31 ns) are shown in Fig. 9 for a power density of 0.9 x $10^{11}$ W/cm$^2$, where the maximum emission is seen at the peak of the pulse. Note the increased emission and narrowing of the UTA with time up to the peak of the pulse.

## Varying pulse duration

In the second survey, laser pulse duration was varied from 7 to 40 ns (FWHM), using the power density with the maximum CE from the first survey (0.8 x $10^{11}$ W/cm$^2$). The relevant data is shown in Table II along with general results (laser energy, CE into $2\pi$ sr, plasma length, *etc*.). As in the first survey, the results are reported for a simulation over the outer 20 cells, the 2% in-band energy was calculated over 20 frequency points, and the plasma length was determined from the position of the last cell in MED103.

The calculated spectra are shown in Fig. 10. Clearly, the in-band emission increases with pulse duration to a maximum at 20 ns, and then decreases again as the number of UTA contributing ions increase and then decrease. The maximum CE was

calculated at a pulse duration of 10 ns, where a CE of 2.29% was obtained, 4% higher than that at 15 ns. Note that the in-band energy increases with increased pulse duration, but the conversion efficiency ultimately decreases beyond 10 ns because of the greater laser energy required to heat the plasma to the optimum electron temperature. The plasma length also increases with longer pulse durations as is to be expected,[31,35] before decreasing at longer pulse durations because of insufficient coupling at the plasma initiation where the steepness of laser pulse leading edge has a major effect on the subsequent plasma expansion velocity.

Experiments using 6 beams of the Nd:YAG Gekko II laser[31] showed that opacity effects are a function of plasma size, and that longer pulse durations produce larger plasmas. A maximum CE of 2.2% was observed at 5.0 x $10^{11}$ W/cm$^2$ and 2.3-ns pulse duration[40], where the EUV emitting region is thinner in shorter pulses, and intensity increased as pulse duration decreased (8.5 to 2.3 ns) before decreasing beyond 1.2 ns.

In an experiment on a 500-μm, spherical, mass-limited microballoon target, an increase in CE was also obtained as the pulse duration decreased.[31,41] It is not clear from that study, however, whether the power density remained constant, *i.e.*, the power density and pulse duration were changed together. In this study, a shorter pulse duration produced a greater CE with the power density kept constant.

Calculations using a 2-D radiative magneto-hydrodynamic code also showed the effect of pulse duration, where the maximum CE was found using a 2.2-ns FWHM flat-top spatial profile pulse at 4.6 x $10^{10}$ W/cm$^2$, a 1.5-fold increase in CE over the comparable 8.0-ns pulse, attributed to less absorption in the lower ion stage wings.[42]

It should be noted that the original duration of 15 ns in the study here was chosen to compare to the Nd:YAG laser available for experiment.[28] A further survey, varying both power density and pulse duration, is required to determine optimum laser parameters for production of in-band radiation.

Further surveys will also investigate the effect of incident wavelength, in particular the lower electron density, lower opacity $CO_2$ LPP, where studies have shown that energy is absorbed in the plasma surface rather than the target surface, in contrast to the more penetrating Nd:YAG LPP, and that for longer-wavelength lasers the dominant absorption process is Joule heating ($\propto \lambda^2$).[43] Opacity effects are much reduced in an optically thin $CO_2$ LPP which can greatly ease computational methods and has been shown to lead to a more than 2-fold increase in CE.[44]

A pre-pulse-pulse setup, where the plasma is primed with an Nd:YAG followed by a $CO_2$ main pulse has also been seen to improve CE to 4% on a 20-μm minimum-mass tin microdroplet (greater than the 2.5% observed from a single $CO_2$ pulse, planar Sn target).[45] Here, the droplet was shown to be too small for optimum laser coupling, but was sufficiently expanded with the Nd:YAG pre-pulse prior to the $CO_2$ main pulse, where the pre-pulse formed a low-density, expanded target which enhances laser absorption.

## VI. CONCLUSION

Previously, to determine emission from a doped-tin target, the oscillator strengths for Sn V – Sn XIV were weighted by the fractional ion density calculated from an optically thin, steady-state plasma model and showed a maximum emission at 40 eV.[13] In

this study, to determine emission from a pure tin target, the oscillator strengths were weighted by the ion density as a function of time and distance, calculated from a 1-D Lagrangian hydrodynamic code and a multi-frequency radiation transport model. Conversion efficiency of laser energy from a 1064-nm laser to in-band emission was determined from two independent parametric studies, and the maximum CE was obtained for a laser power density of 0.8 x $10^{11}$ W/cm$^2$ and a pulse duration of 10 ns, though the power density in the 1-D case likely underestimates the required experimental power density to reproduce the modelled conditions for maximum CE, due to the absence of lateral expansion in the 1-D model and plasma-target interactions.

## ACKNOWLEDGMENTS

This work was supported by Science Foundation Ireland under Investigator Grant 07/IN.1/B1771, COST Action MP0601, Intel Ireland and the Irish Research Council for Science, Engineering and Technology.

[1] D. Attwood, J. Phys. D **37**, Editorial (2004).

[2] F. Jin and M. Richardson, *Appl. Opt*. **34,** 5750 (1995).

[3] C. Cerjan, *Appl. Opt*. **32,** 6911 (1993).

[4] G. O'Sullivan, A. Cummings, P. Dunne, P. Hayden, L. McKinney, N. Murphy and J. White, *EUV Sources for Lithography*, editor Vivek Bakshi, Publ., SPIE (2005).

[5] A. Cummings, G. O'Sullivan, P. Dunne, E. Sokell, N. Murphy, and J. White, J. Phys. D **38**, 604 (2005).

[6] M. C. Richardson, C.-S. Koay, K. Takenoshita, C. Keyser, B. Bernath, S. A. George, and S. Teerawattanasook, Proc. SPIE **5580**, 434 (2005).

[7] T. Aota and T. Tomie, Phys. Rev. Lett. **94**, 015004 (2005).

[8] P. K. Carroll and G. O'Sullivan, Phys. Rev. A **25**, 275 (1982).

[9] W. Svendsen and G. O'Sullivan, Phys. Rev. A **50**, 3710 (1994).

[10] G. O'Sullivan and R. Faulkner, Opt. Eng. **33**, 3978 (1994).

[11] R. D. Cowan, *The theory of atomic structure and spectra*, Berkeley, University of California Press, 1981.

[12] J. Bauche and C. Bauche-Arnoult, Phys. Scr. **T40**, 58 (1992).

[13] J. White, P. Hayden, P. Dunne, A. Cummings, N. Murphy, P. Sheridan, and G. O'Sullivan, J. Appl. Phys. **98**, 113301 (2005).

[14] D. Colombant and G. F. Tonon, J. Appl. Phys. **44**, 3524 (1973).

[15] J. White, A. Cummings, P. Dunne, P. Hayden, and G. O'Sullivan, J. Appl. Phys. **101**, 043301 (2007).

[16] M. Itoh, T. Yabe, and S. Kiyokawa, Phys. Rev. A **35**, 233 (1987).

[17] A. Sasaki, K. Nishihara, F. Koike, T. Kagawa, T. Nishikawa, K., Fujima, T. Kawamura, and H. Furukawa, J. Sel. Top. Quant. Elec. **10,** 1307 (2004).

[18] J. Bauche and C. Bauche-Arnoult, Physica Scripta **37**, 659 (1988).

[19] P. K. Patel, J. S. Wark, O. Renner, A. Djaoui, S. J. Rose, D. J. Heading, and A. Hauer, J. Quant. Spectrosc. Radiat. Transfer **58**, 835 (1997).

[20] A. Djaoui, Rutherford Appleton Laboratory report: *RAL-TR-96-099*, RAL, Didcot, U.K. (1996).

[21] J. P. Christiansen, D. E. T. F. Ashby, and K. V. Roberts, Computer Physics Communications, **7** (1974).

[22] R. M. More, J. Quant. Spectrosc. Radiat. Transfer **27**, 345 (1982).

[23] P. K. Patel, J. S. Wark, D. J. Heading, A. Djaoui, S. J. Rose, O. Renner, and A. Hauer, J. Quant. Spectrosc. Radiat. Transfer **57**, 683 (1997).

[24] A. Djaoui, S. J. Rose, and J. S. Wark, J. Quant. Spectrosc. Radiat. Transfer, **52**(5), 531 (1994).

[25] J. S. Wark, O. Renner, A, Djaoui, S. J. Rose, T. Missalla, D. Neely, E. Foerster, and A. J. Hauer, Quant. Spectrosc. Radiat. Transfer, **54**(1/2), 419 (1995).

[26] G. Tallents, "Atomic processes in high density plasmas," QuAMP II, Summer School, Open University, Milton Keynes, September 19 (2005).

[27]J. S. Wark, A. Djaoui, S. J. Rose, H. He, O. Renner, O., T. Missalla, and E. Foerster, Phys. Rev. Letters, **72** (12), 1826 (1994).

[28]P. Hayden, A. Cummings, N. Murphy, G. O'Sullivan, P. Sheridan, J. White, and P. Dunne, J. Appl. Phys., **99**, 093302 (2006).

[29]O'Sullivan, G, in *Giant Resonances in Atoms, Molecules and Solids*, eds. Connerade, J. P., Esteva, J. M., and Karnatak, R. C., Plenum New York and London, 505, 1987.

[30]M. Lysaght, D. Kilbane, N. Murphy, A. Cummings, P. Dunne, and G. O'Sullivan, Phys. Rev. A **72**, 014502 (2005).

[31]S. Fujioka, H. Nishimura, K. Nishihara, A. Sasaki, A. Sunahara, T. Okuno, N. Ueda, T. Ando, Y. Tao, Y. Shimada, K. Hashimoto, M. Yamaura, K. Shigemori, M. Nakai, K. Nagai, T. Norimatsu, T. Nishikawa, N. Miyanaga, Y. Izawa, and K. Mima, Phys. Rev. Lett., **95**, 235004 (2005).

[32]O. Morris, P. Hayden, F. O'Reilly, N. Murphy, and P. Dunne, J. Appl. Phys, **91**, 081506 (2007).

[33]P. K. Patel, E. Wolfrum, O. Renner, A. Loveridge, R. Allott, D. Neely, S. J. Rose, and J. S. Wark, J. Quant. Spectrosc. Radiat. Transfer, **65**, 429 (2000).

[34]A. Cummings, G. O'Sullivan, P. Dunne, E. Sokell, N. Murphy, and J. White, J. Phys. D: Appl. Phys., **38**, 604 (2005).

[35]Y. Tao, H. Nishimura, T. Okuno, S. Fujioka, N. Ueda, M. Nakai, K. Nagai, T. Norimatsu, N. Miyanaga, K. Nishihara, Y. Izawa, and Y. Izawa, Appl. Phys. Lett., **87**, 241502 (2005).

[36]Yamuara, M, Uchida, S., Sunahara, A., Shimada Y., Nishimura, H., Fujioka, S., Okuno, T., Hashimoto, K., Nagai, K., Norimatsu, T., Nishihara, K., Miyanga, N., Izawa, Y., & Yamanaka, C., Characterization of extreme ultraviolet emission using the fourth harmonic of a Nd:YAG laser, *Appl. Phys. Lett*. **86**, 181107 (2005).

[37]Sequoia, K.L., Tao, Y., Yuspeh, S., Burdt, R., & Tillack, M.S., Two dimensional expansion effects on angular distribution of 13.5 nm in-band extreme ultraviolet emission from laser-produced Sn plasma, *Appl. Phys. Lett*. **92**, 221505 (2008).

[38]S. Düsterer, H. Schoerer, W. Ziegler, C. Ziener, and R. Sauebrey, *Applied Physics B* **73**, 693–698 (2001).

[39]S. Goldsmith, J. C. Moreno, and H. R. Griem, J. Appl. Phys., **64** (2) (1988).

[40]T. Ando, T., S. Fujioka, H. Nishimura, N. Ueda, Y. Yasuda, K. Nagai, T. Norimatsu, M. Murakami, K. Nishihara, N. Miyanaga, Y. Izawa, and K. Mima., K., *Appl. Phys. Lett.* **89**, 151501 (2006).

[41]J. J. MacFarlane, C. L. Rettig, P. Wang, I. E. Golovkin, and P. R. Woodruff, in *Emerging Lithographic Technologies IX*, Mackay, R.S., editor; SPIE-Int Society Optical Engineering: Bellingham, Vol. 5751, 588 (2005).

[42]J. White, G. O'Sullivan, S. Zakharov, P. Choi, V. Zakharov, H. Nishimura, S. Fujioka, and K. Nishihara, J. Appl. Phys, **92**, 151501 (2008).

[43]A. Takahashi, D. Nakamura, K. Tamaru, T. Akiyama, and T. Okada, *Appl. Phys. B* **92**, 73–77 (2008).

[44]J. White, P. Dunne, P. Hayden, F. O'Reilly, and G. O'Sullivan, *Appl. Phys. Lett*. **90**, 181502 (2007).

[45]S. Fujioka, H. Nishimura, M. Shimomura, H. Sakaguchi, Y. Nakai, T. Aota, Y. Shimada, A. Sunahara, and K. Nishihara, Journal of Physics: Conference Series **112** 042049 (2008).

TABLE I Results of power density survey: 0.5–1.5 x $10^{11}$ W/cm$^2$

(1064 nm, 15 ns FWHM, cylindrical geometry, 90 μm radius)

| Run | Wave-length (nm) | Duration (ns) FWHM | Pequiv (x $10^{11}$ W/cm$^2$) | Elaser (mJ) | CE (% per 2π sr) | Plasma length (mm) | max $T_e$ (eV) | max <z> |
|---|---|---|---|---|---|---|---|---|
| A1 | 1064 | 15 | 0.5 | 191 | 1.03 | 2.90 | 21.9 | 8.6 |
| A 2 | 1064 | 15 | 0.6 | 229 | 1.58 | 3.11 | 24.8 | 9.9 |
| A 3 | 1064 | 15 | 0.7 | 267 | 2.01 | 3.26 | 28.0 | 11.1 |
| A 4 | 1064 | 15 | 0.8 | 305 | 2.21 | 3.47 | 31.0 | 12.2 |
| A 5 | 1064 | 15 | 0.9 | 344 | 2.16 | 3.68 | 34.3 | 13.2 |
| A 6 | 1064 | 15 | 1.0 | 382 | 1.84 | 3.81 | 37.8 | 14.2 |
| A 7 | 1064 | 15 | 1.1 | 420 | 1.48 | 3.89 | 41.4 | 15.1 |
| A 8 | 1064 | 15 | 1.3 | 496 | 1.06 | 4.20 | 48.4 | 16.7 |
| A 9 | 1064 | 15 | 1.5 | 573 | 0.92 | 4.78 | 60.4 | 18.7 |

TABLE II Results of pulse duration survey: 7–40 ns (FWHM)

(1064 nm, 0.8 x $10^{11}$ W/cm$^2$, cylindrical geometry, 90 μm radius)

| Run | Wave-length (nm) | Duration (ns) FWHM | Pequiv (x $10^{11}$ W/cm$^2$) | Elaser (mJ) | CE (% per 2π sr) | Plasma length (mm) | max $T_e$ (eV) | max <z> |
|---|---|---|---|---|---|---|---|---|
| B1 | 1064 | 7 | 0.8 | 143 | 1.93 | 1.94 | 26.6 | 9.4 |

| | | | | | | | | |
|---|---|---|---|---|---|---|---|---|
| B2 | 1064 | 10 | 0.8 | 204 | 2.29 | 2.39 | 29.6 | 11.2 |
| B3= A4 | 1064 | 15 | 0.8 | 305 | 2.21 | 3.47 | 31.0 | 12.2 |
| B4 | 1064 | 20 | 0.8 | 407 | 1.71 | 4.07 | 36.0 | 13.6 |
| B5 | 1064 | 23 | 0.8 | 468 | 1.16 | 4.20 | 36.6 | 14.0 |
| B6 | 1064 | 30 | 0.8 | 611 | 0.51 | 3.91 | 38.0 | 14.5 |
| B7 | 1064 | 40 | 0.8 | 814 | 0.29 | 3.29 | 38.5 | 14.7 |

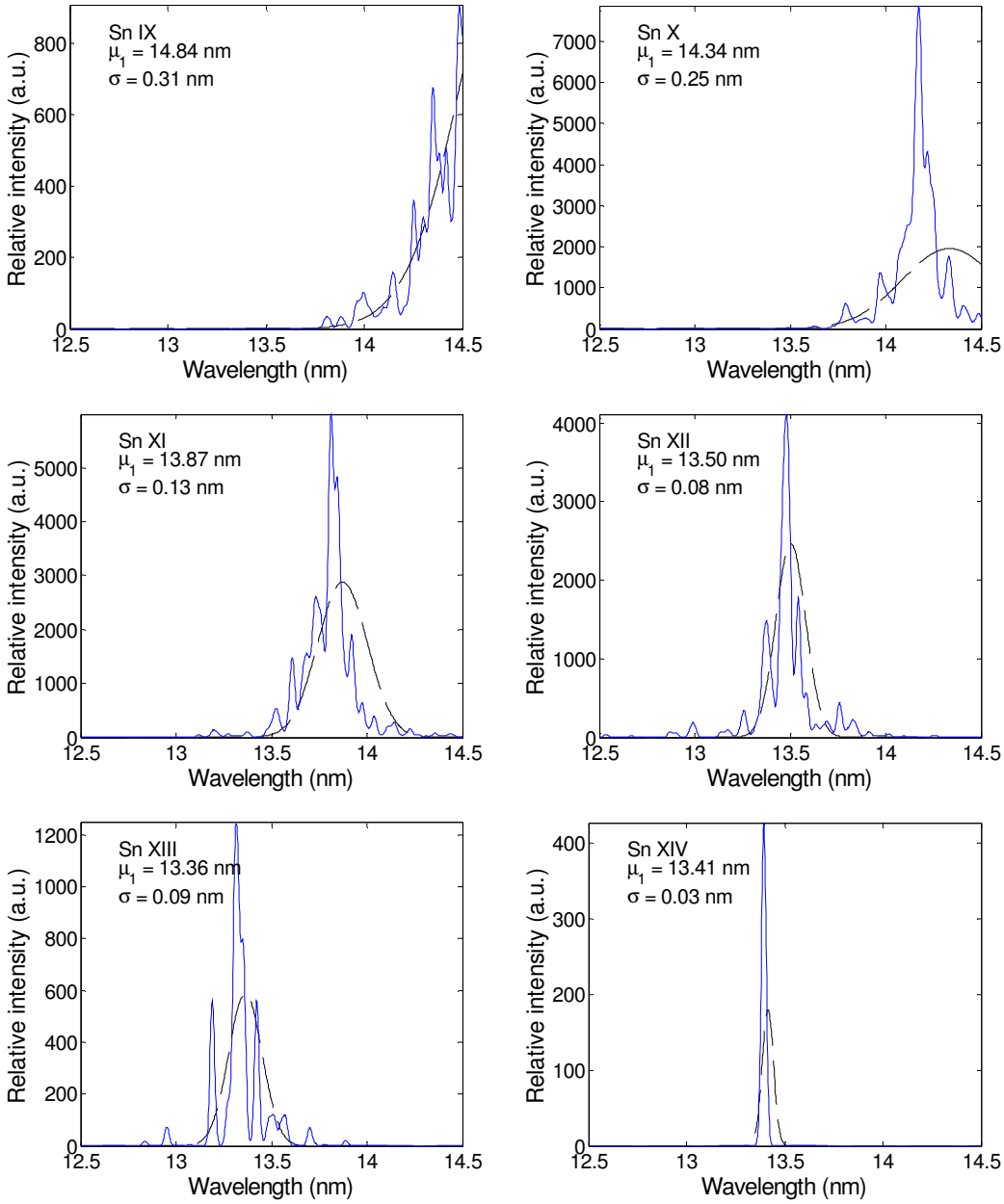


FIG. 1. *gf* values convolved with a Gaussian profile (solid) and statistical UTA (dashed) from Sn IX to Sn XIV for 4d-4f transitions.

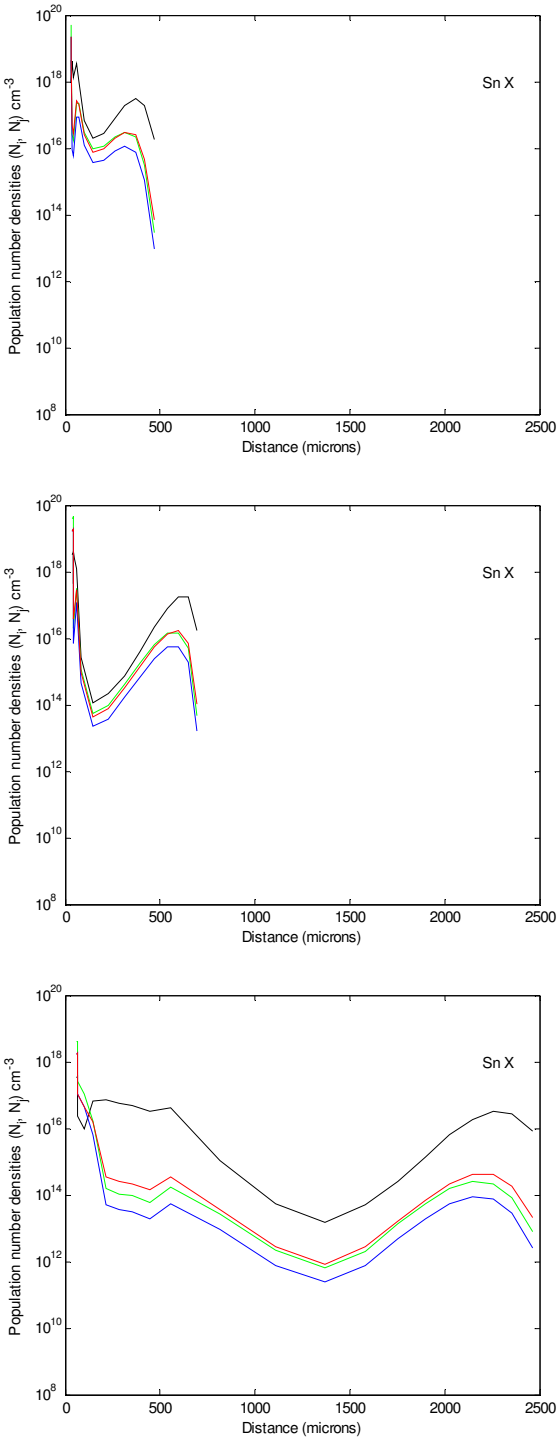


**Figure 2 Sn X level populations versus distance before, at, and after the peak of the pulse (49 ns)**

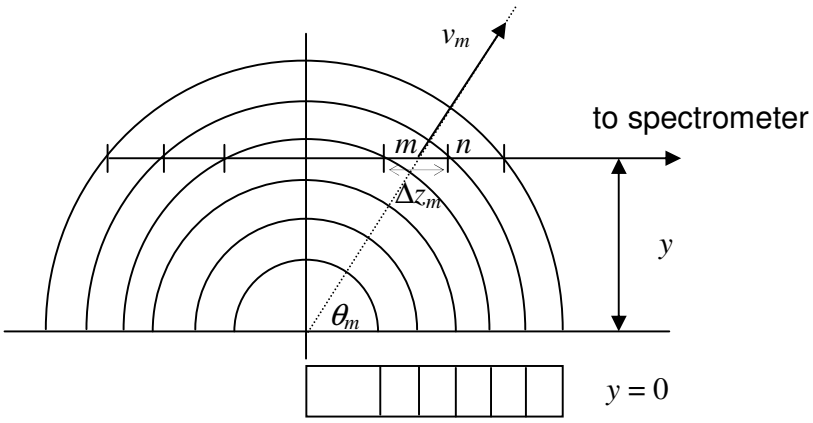


**Figure 3 Schematic view of cross-section through cylinder**

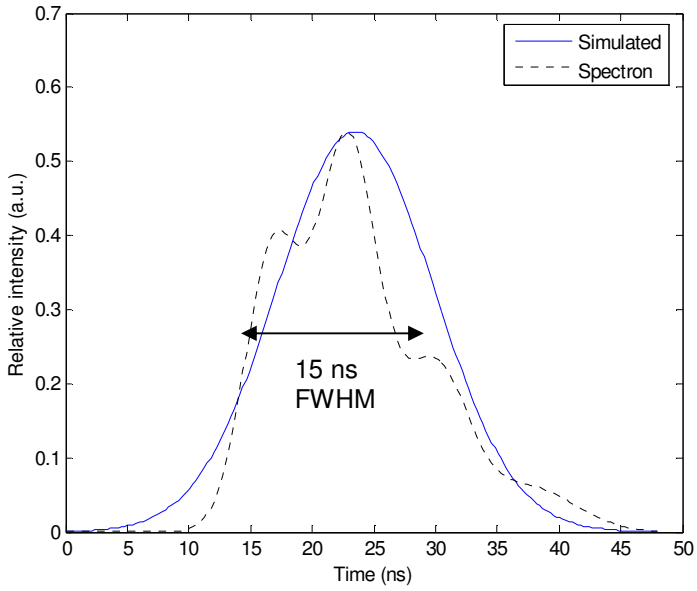


**Figure 4 Multiple-Gaussian (dashed) and simulated Medusa single-Gaussian (solid) laser pulse**

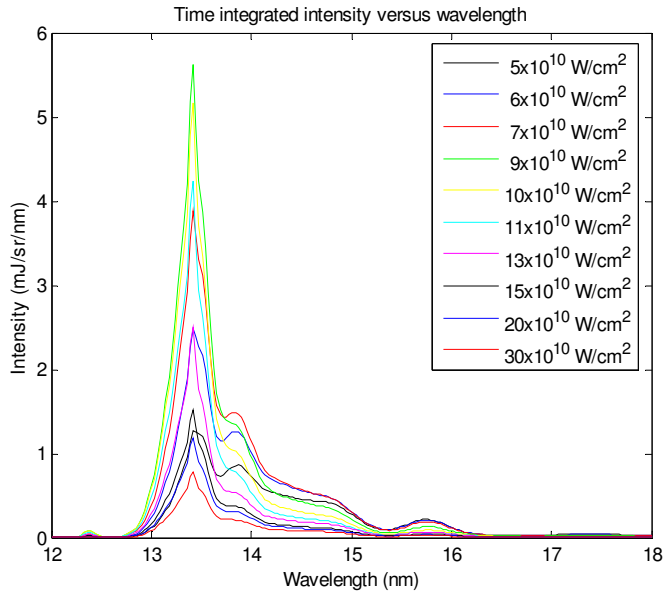


**Figure 5 Calculated spectra at different laser power densities (0.5–3.0 x $10^{11}$ W/cm$^2$ for 1064 nm, 15 ns FWHM, cylindrical geometry, 90 μm radius, 20 cell simulation)**

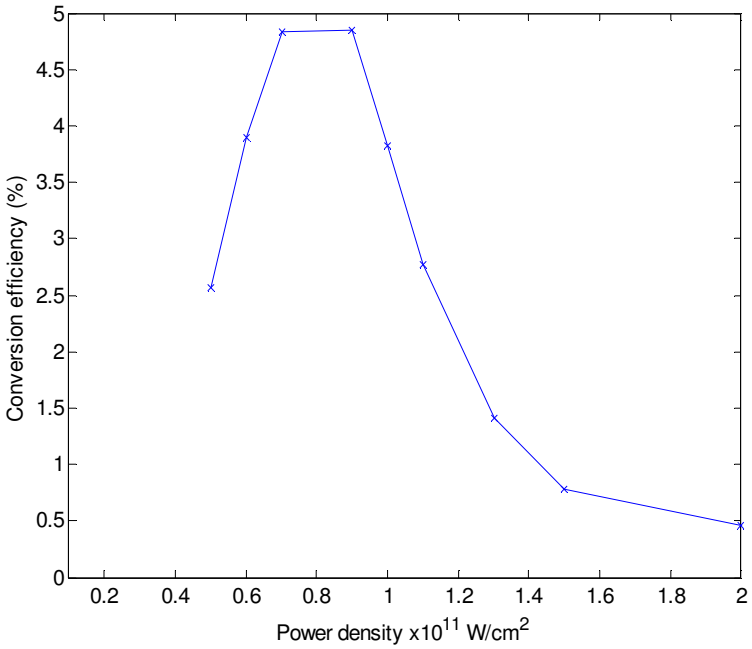


**Figure 6 Conversion efficiency versus laser power density (0.5 to 2.0 x $10^{11}$ W/cm$^2$ for 1064 nm, 15 ns FWHM, cylindrical geometry, 90 μm radius, 20 cell simulation)**

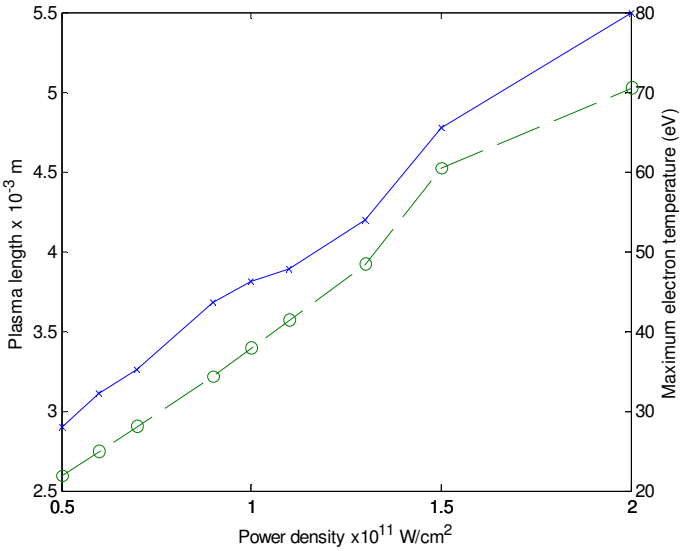


**Figure 7 Plasma length (x) and maximum electron temperature (o) versus power density (0.5 to 2.0 x $10^{11}$ W/cm$^2$ at 1064 nm, 15 ns FWHM, cylindrical geometry, 90 µm radius, 20 cell simulation)**

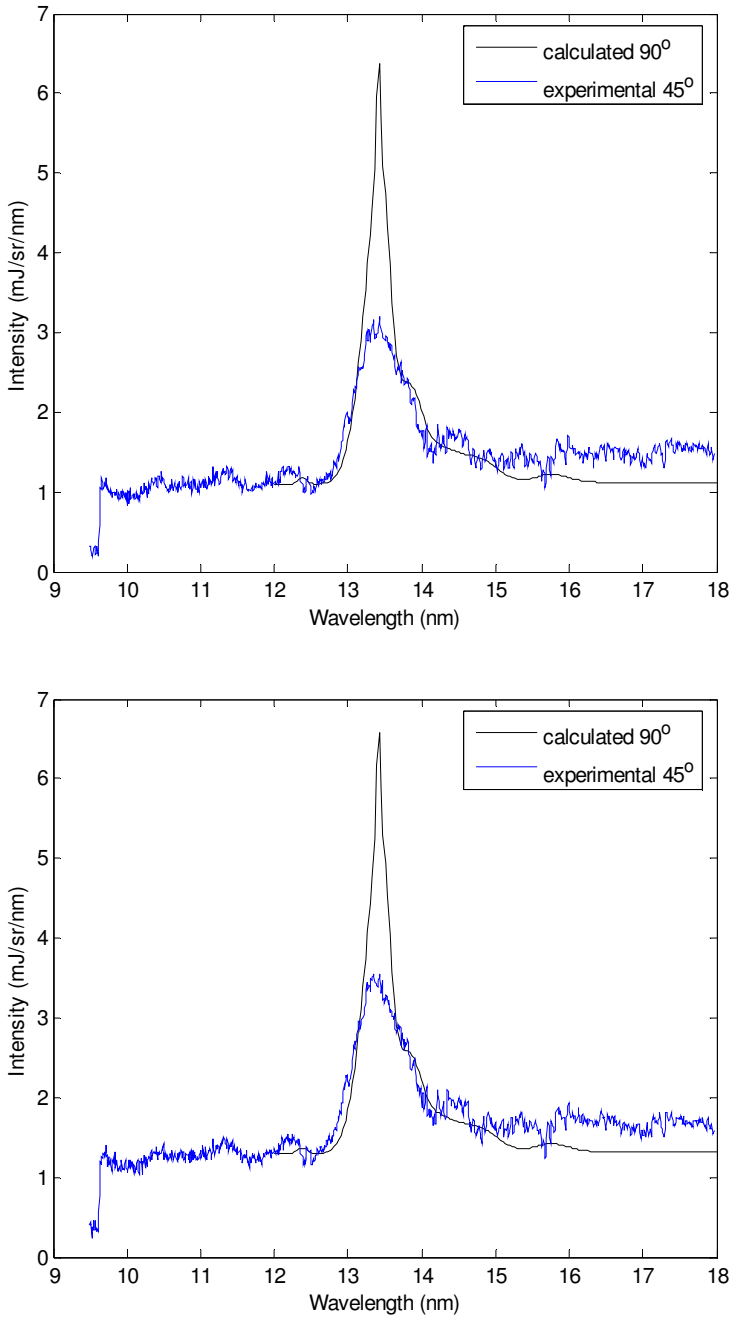


**Figure 8 Calculated 0.9 x $10^{11}$ W/cm$^2$ versus experimental 0.82 x $10^{11}$ (top) and 0.91 x $10^{11}$ W/cm$^2$ (bottom) spectra (1064 nm, 15 ns FWHM, cylindrical geometry, 90 μm radius, 20 cell simulation)**

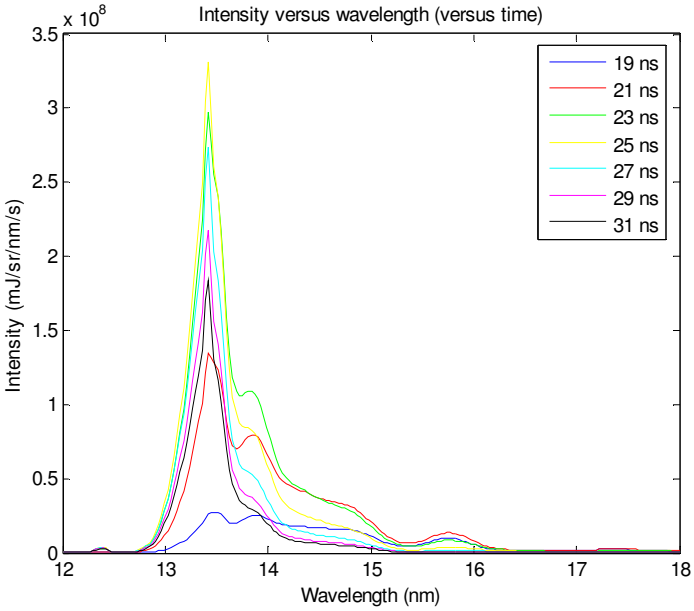


**Figure 9 Spectra versus selected times (19–31 ns) (0.9 x $10^{11}$ W/cm$^2$ at 1064 nm, 15 ns FWHM, cylindrical geometry, 90 μm radius, 20 cell simulation**

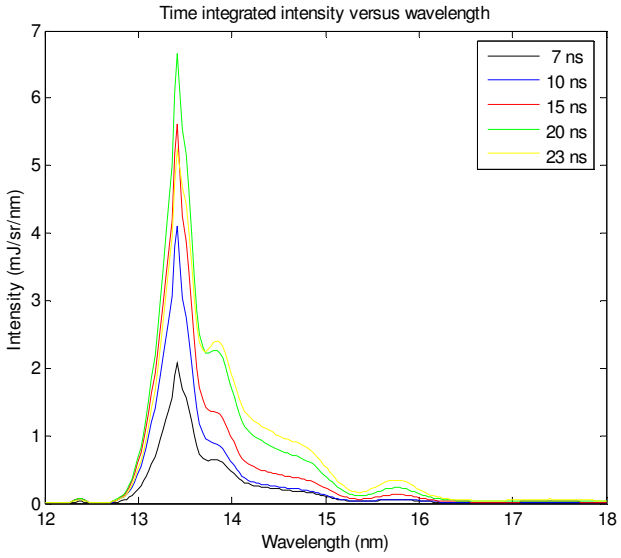


**Figure 10 Calculated spectra at different pulse lengths (7 to 23 ns (FWHM) for1064 nm, 0.9 x $10^{11}$ W/cm$^2$, cylindrical geometry, 90 μm radius, 400 cell simulation)**